



This is the accepted manuscript made available via CHORUS. The article has been published as:

Spatially dispersive helicity-dependent photocurrent in Dirac semimetal Cd_3As_2 nanobelts

Bob Minyu Wang, Yuqing Zhu, Henry Clark Travaglini, Renzhi Sun, Sergey Y. Savrasov, William Hahn, Klaus van Benthem, and Dong Yu

Phys. Rev. B **108**, 165405 — Published 5 October 2023

DOI: [10.1103/PhysRevB.108.165405](https://doi.org/10.1103/PhysRevB.108.165405)

Spatially Dispersive Helicity Dependent Photocurrent in Dirac Semimetal Cd₃As₂ Nanobelts

Bob Minyu Wang,¹ Yuqing Zhu,¹ Henry Clark Travaglini,¹ Renzhi Sun,¹
Sergey Y. Savrasov,¹ William Hahn,² Klaus van Benthem,² and Dong Yu^{1,*}

¹*Department of Physics and Astronomy, University of California, Davis*

²*Department of Materials Science and Engineering, University of California, Davis*

Topological insulators and Weyl semimetals have demonstrated helicity-dependent photocurrent (HDPC). In contrast, Dirac semimetals (DSMs) possess chirality-degenerate Weyl nodes and were thought to forbid HDPC, unless the symmetry is broken by external stimulus such as strain. Here, we demonstrate HDPC in strain-free DSM Cd₃As₂ nanobelt field effect transistors at room temperature. Free-standing single-crystalline Cd₃As₂ nanobelts grown by chemical vapor deposition allows fabrication of devices without the complication of external strain. HDPC mapping with micrometer resolution reveals HDPC in the vicinity of the metal contact. We attribute the HDPC to the spin-polarized Fermi arcs at the surface, supported by theoretical calculation, as well as photon energy and angle-resolved helical photocurrent mapping. This work provides key insights on light polarization controlled spin manipulation in Dirac materials.

I. INTRODUCTION

Thanks to their unique linear dispersion relation, spin-momentum locking, and forbidden charge carrier back-scattering, topological materials have skyrocketed in popularity over the past few decades, demonstrating promising potential for low-dissipation and paradigm-shifting applications in spintronics [1] and quantum computations [2]. As an important member of the topological material family, Dirac semimetals (DSMs) have demonstrated exotic properties such as high carrier mobility [3], 3D quantum Hall effect [4], topologically protected spin transport [5], giant magnetoresistance [6], and topological superconductivity [7–9]. However, as the DSMs exhibit high crystal symmetry, Weyl nodes of opposite chirality are paired up at the same position in k -space, thus cancelling their corresponding Berry fluxes. Consequently, unlike some other topological materials such as topological insulators (TIs) and Weyl semimetals (WSMs), direct electrical spin generation [10] in DSMs is forbidden by this spin degeneracy, limiting their more widespread use in spintronic and quantum device applications.

An alternative route of spin control is via circularly polarized light. The circular photogalvanic effect (CPGE) has been demonstrated in TIs [11–13] and WSMs [14]. It has been recently realized that CPGE directly measures the topological charge of Weyl points, quantized to a material-independent value [15]. Fundamentally, CPGE relies on asymmetric contributions to photocurrent from incident helical photons. However, DSMs, obeying crystal inversion and time reversal symmetry, were believed to be strictly forbidden to manifest CPGE [16]. Indeed, to date, CPGE has not been experimentally demonstrated in DSMs, except in the case that the crystal symmetry is reduced by external strain [17]. Nevertheless,

here we experimentally demonstrate unambiguous signatures of CPGE observed in strain-free DSM Cd₃As₂ nanobelt field effect transistors (FETs). CPGE can be clearly observed at the interface made by 100-nm thick Cd₃As₂ nanobelts and the metal contact. This work not only provides key insights on understanding spin generation and transport in DSMs, but also broadens the material basis to include apparently spin degenerate Dirac materials for potential spin-related applications.

II. METHODS

A. Synthesis, characterization, and device fabrication

Our Cd₃As₂ nanobelts were grown by chemical vapor deposition (CVD) following a recipe adapted from previous reports [18–20]. Briefly, Cd₃As₂ lumps and powder (99% purity, Alfa Aesar) were placed 10 cm upstream from the center of a quartz tube within a Lindberg tube furnace, ramped to 640°C, and held for 35 minutes. Ar gas flowing at 20–30 sccm carried vapor 15 cm downstream to a Si substrate where deposition occurred at 200–250°C. The silicon wafer was elevated to the center of the tube using a quartz platform. Cd₃As₂ nanobelts were cast onto 200 mesh copper grids covered with an amorphous carbon film and characterized with a Jeol JEM 2100F/AC TEM operated at 200 keV. Electron diffraction patterns of bulk Cd₃As₂ were calculated under the assumption of kinematical diffraction conditions using the CrystalMaker software package.

These free-standing nanobelts were then mechanically transferred to 300 nm SiO₂ covered Si chips by gently stamping the Si chip onto the as-grown substrate. The applied force was largely from the mass of the chip, about 60 mg. Only a weak Van der Waals force is expected from the amorphous substrate, which may apply a small strain at the bottom of the nanobelts. The nanobelts in

* yu@physics.ucdavis.edu

our studies were also straight, and hence were not under strain as in bent nanoribbons [21]. Furthermore, the thickness of our nanobelts was about 100 nm, which was much thicker than the optical penetration depth (about 20 nm). So most of the CPGE action occurs near the top surface of the nanobelts, which is believed to be free of strain as a result. In comparison, the previous work demonstrating CPGE in Cd_3As_2 is based on a 20 nm thick film epitaxially grown on GaAs substrates, where a large strain is expected [17]. Thicker films showed much weaker CPGE in their work. FETs incorporating single nanobelts were fabricated by standard e-beam lithography (EBL, FEI 430 NanoSem) with 5 nm Cr / 295 nm Au as contacts deposited by e-beam evaporation. As acetone is hygroscopic and Cd_3As_2 is sensitive to water exposure, only water-free acetone was used to perform lift off.

B. Circularly polarized scanning photocurrent microscopy

Spatially resolved optoelectronic measurements were performed at room temperature using a 532 nm continuous wave laser focused by a $10\times$ N.A. 0.25 objective lens, perpendicular to the channel with an oblique incident angle of $\theta = 45^\circ$. Photocurrent images were obtained by raster-scanning the laser on the device plane using a pair of mirrors mounted on galvanometers. Photocurrents were measured as a function of laser position and photon polarization through a DL1211 preamplifier followed by a LabView data acquisition board. Low temperature measurements were performed in a Janis ST-500 optical cryostat. We found that the laser spot on the sample was highly elongated to a $2.5 \times 40 \mu\text{m}^2$ area, as determined from the photocurrent image. This elongation is a result of astigmatism caused by oblique incidence through the quartz window of the cryostat [22]. Spatial resolution was maximized along the device channel by focusing the short axis of the elongated laser spot along the channel.

Circularly polarized light was achieved by passing a linearly polarized beam through a rotating zero-order quarter waveplate (QWP) at 532 nm (Thorlabs). The output polarization is a function of the angle between the fast axis of the QWP and the incident linear polarization (α), continuously changing between left circular polarization (LCP) at 45° and 225° , to linear polarization (LP) at 0° , 90° , 180° , and 270° , and to right circular polarization (RCP) at 135° and 315° as the QWP is rotated. To obtain spatial resolution, photocurrent maps were taken in 5° increments in α . Then, the photocurrent as a function of α was constructed at every pixel in the map. A Python program is finally used to fit the photocurrent at each pixel to Eqn. 1 to extract C and D maps. Photon energy dependence measurements were performed using a tunable laser (NKT Photonics) and achromatic QWPs (Thorlabs). The laser was focused at the contact and photocurrent was measured as the QWP was rotated.

The cryostat window was removed for the room-temperature incident angle dependence measurements to avoid the beam astigmatism. Different θ angles were achieved by rotating the cryostat while ensuring that the device served as the center of rotation. We acknowledge that the focused light through the objective lens introduces an uncertainty in the incidence angle equivalent to the cone half angle on either side of optic axis. We estimate this error to be $\pm 7^\circ$ in our measurements, significantly smaller than the range of θ achieved in our experiments. ϕ dependence was performed by rotating the sample inside the cryostat.

III. RESULTS

A. Nanobelt growth and field effect characteristics

Our Cd_3As_2 growths yielded both nanowires and nanobelts as shown in Fig. 1(a). We have observed that adjusting the Ar flow rate could produce more nanobelts than nanowires as previously reported [19]. The nanobelts, which we focus on studying here, typically have thickness 80-100 nm, length 10-60 μm , and width 3-10 μm . Energy dispersive X-ray spectroscopy (EDS) confirmed correct and uniform stoichiometry along the nanobelts [Fig. 1(b) inset]. Powder X-ray diffraction (XRD) on an as-grown sample indicated the nanobelts were dominantly the body centered tetragonal centrosymmetric $I4_1/acd$ (142) phase [23], though there might exist a small portion of the nanostructures belonging to the $P4_2/nbc$ (133) phase [20] implied by a small peak at $2\theta = 33^\circ$ [Fig. 1(b)].

Cd_3As_2 nanostructures have been reported to grow in one of two directions, $\langle 112 \rangle$ or $\langle 110 \rangle$ [24]. Selected area electron diffraction (SAED) was performed in a transmission electron microscope (TEM) to determine the growth direction of our nanostructures, which was found to be along the $[112]$ direction. It should be noted that the bright spot between spots labeled (112) and (116) in Fig. 1(c) is not reproduced by kinematical diffraction calculations [Fig. 1(f)]. Forbidden reflections in the experimental data result from dynamic scattering - multiple scattering effects - as the thickness of the nanobelt in the electron beam direction is significantly larger than the elastic mean free path length for electrons accelerated to 200 keV. The morphology of the nanobelts observed by TEM and a correlation with previous studies suggest that that surface plane is orthogonal to the growth direction and therefore belongs to $\{110\}$ [23].

FETs incorporating single nanobelts were then fabricated by standard e-beam lithography. Current vs. source-drain bias (I - V_b) curves were linear and the conductance increased at positive gate voltage (V_g) [Fig. 1(e)], indicating an n -type channel. The conductance slightly increased at negative V_g at 78 K, implying the Fermi level can be tuned below the Dirac point. Field-effect electron mobilities (μ) were extracted to be 3500

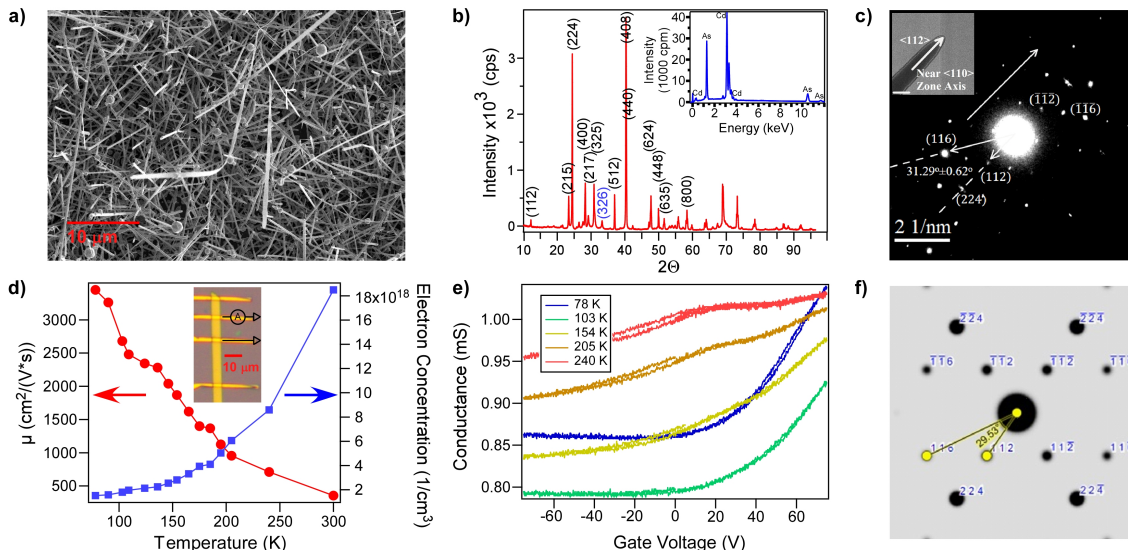


FIG. 1. Cd_3As_2 nanobelts and device characteristics. (a) Scanning electron microscopic (SEM) image of a representative as-grown sample containing a high density of nanowires and nanobelts. (b) Powder XRD spectrum of Cd_3As_2 nanobelts on an as-grown substrate, in agreement with the (142) phase. A small peak indicated by (326) in blue implies the existence of a mixed phase (133). Inset: EDS of the sample. (c) SAED pattern of the nanobelt recorded near the $\langle 110 \rangle$ zone axis orientation. Inset: Bright field TEM image of a representative nanobelt supported by amorphous carbon. (d) Electron mobility and concentration versus temperature, extracted from field effect measurements in the linear regime at positive gate voltage. Inset: Optical image of Device #1. (e) Conductance versus gate voltage at various temperatures. (d) and (e) were taken in Device #1. (f) Calculated bulk diffraction pattern in the $\langle 110 \rangle$ zone-axis orientation reproducing the SAED results in (c).

cm^2/Vs at 78 K in the linear regime with the steepest slope [Fig. 1(d)] in this device (Device #1). Apparent field-effect mobilities extracted in different gate voltage regimes are shown in Fig. 7. Up to $1.01 \times 10^4 \text{ cm}^2/\text{Vs}$ were extracted in other devices (Table I). The measured μ is comparable to that in bulk Cd_3As_2 crystals [3] and demonstrates the high quality of the nanobelts. When the temperature was increased from 78 K to 300 K, μ decreased by two orders of magnitude and the electron concentration increased by one order of magnitude.

B. Helicity dependent photocurrent measurements

Photocurrent mapping revealed large photocurrent only near the contacts, each exhibiting opposite polarities [Fig. 2(b)]. The localized photocurrent is different from the nonlocal distribution in Sb doped Bi_2Se_3 devices [25], presumably caused by a combination of the fast carrier recombination in the semimetal and local dissipation through the gapless bulk states. The photocurrent can be generated by photovoltaic (PV) and photo-thermoelectric (PTE) mechanisms [26]. The photocurrent sign is consistent with an n -type channel where band-bending is upward to the metal contact. The internal quantum efficiency (IQE) is estimated to be about 0.1%.

The dependence of photocurrent distributions on α can be clearly detected, as shown in Fig. 2(c). The photocurrent differs under LCP and RCP [Fig. 2(d)], only when

the photoexcitation is close to the contacts. The photocurrent profiles at each laser position are fit by Eqn. (1) to extract modulation amplitudes,

$$I = C \sin(2\alpha) + L_1 \sin(4\alpha) + L_2 \cos(4\alpha) + D \quad (1)$$

where C represents the amplitude of HDPC, L_1 the linear polarization dependent effects, L_2 the reflectance difference at s and p polarizations, and D the polarization independent contributions. We estimate the HDPC per incident photoexcitation power to be 13 nA/mW in our devices. This is similar to the value reported in the 20 nm epitaxially grown thin film but much larger than that observed in the 150 nm film [17], indicating that the HDPC observed in our 100 nm thick CVD-grown nanobelts is unlikely caused by strain.

The distributions of C and D are shown in Fig. 2(e). Here we focus on C which is directly related to HDPC. One striking observation is that C is only large when the laser is focused close to the metal-semimetal interface, as shown in Fig. 2(e). This is different from the previous observations in TIs, where the distributions of C were found to be relatively uniform along the channel [11, 13]. The Au contact is thick enough to block the photon penetration, consistent with the fact that the largest C appears near the Au contact where photons can be absorbed by the nanobelt. Interestingly, C has the same sign at opposite contacts in the device channel, but switches sign outside of the channel. The signs

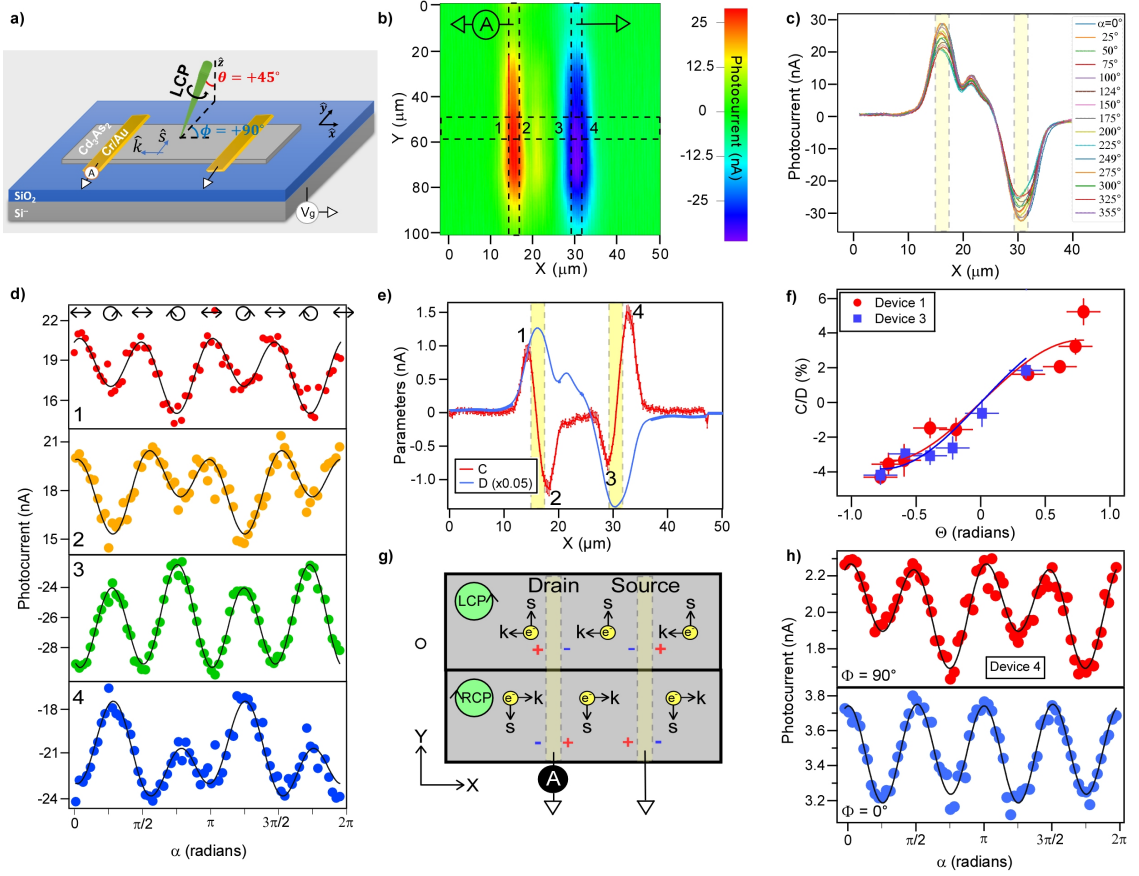


FIG. 2. Spatially resolved HDPC measurements at room temperature. (a) Schematic of measurement configuration. The data in (b)-(e) were taken with the laser incident in the y - z plane at $\theta = 45^\circ$ and $\phi = 90^\circ$ as indicated. (b) Short-circuit photocurrent map. '1'-'4' denote positions where HDPC is strongest. The vertical dashed rectangles denote the metal contact positions, while the horizontal dashed rectangle denotes the size of the nanobelt. The incident laser intensity was 145 W/cm^2 . (c) Photocurrent cross sections along the channel at different α . Dashed rectangles denote the contact positions. (d) Photocurrent at positions '1'-'4' as a function of α . Solid curves are fittings by Eqn. (1). (e) Cross sections of extracted C and D (scaled down) along the channel with positions '1'-'4' denoted. (f) θ dependence of C/D for two representative devices. The solid curve is a fit by Eqn. (2). (g) Schematic depicting the polarity of helical photocurrent. Electron spin (s) is injected in-plane through oblique incidence. k indicates the momentum locked to the injected spin. + (increase) and - (decrease) indicate the modulation to the photocurrent caused by spin-momentum coupling. (h) Photocurrent modulation at different ϕ values. Note that π periodicity vanishes with in-plane spin longitudinal to the channel. (b)-(e) were taken from Device #2, (f) from #1 and #3, (h) from #4.

of C at different locations are consistent with the spin-momentum locking picture depicted in Fig. 2(g). C can be represented by the difference in photocurrent under LCP and RCP photoexcitation. An LCP photon generates an electron with an in-plane spin corresponding to a negative k_x momentum. If generated inside the device channel near the left contact (position '2'), this electron tends to move towards the drain connected to the preamplifier, resulting in a photocurrent smaller than that generated by an RCP photon at this location, leading to a negative C . When the laser is moved out of the channel (position '1'), an LCP generated electron instead has a higher chance of moving away from the drain contact. As a result, the sign of C is flipped. The signs of C for positions C and D are also consistent with this picture. The C distributions and the sign-flipping were highly reproducible in more than 10 devices measured to date.

Also note that the D profile shows a bump in the channel at about $x = 20 \mu\text{m}$ in Fig. 2(e), which is likely caused by the impurity induced local potential fluctuation [27]. However, there is no peak in the C profile at this location, suggesting the generation mechanism of C is different from that for D .

The observed HDPC is highly sensitive to θ as shown in Fig. 2(f). The magnitude of C becomes small at normal incidence and increases with θ . This is expected as normal incidence does not produce in-plane spins needed to modulate the photocurrent. The in-plane spin is flipped at negative θ , leading to momentum reversal and a sign change in HDPC, also consistent with the experimental observations. Quantitatively, the θ dependent HDPC follows reasonably well with the expectation from the polarization dependent optical absorption [Fig. 2(f)] by the

following equation [28],

$$J_{CPGE} = \frac{4E_0^2 \gamma P_{circ} \sin \theta \cos^2 \theta}{n(\cos \theta + \sqrt{n^2 - \sin^2 \theta})(n^2 \cos \theta + \sqrt{n^2 - \sin^2 \theta})} \quad (2)$$

where E_0 is the optical electric field amplitude, γ is the spin-orbit coupling constant, $P_{circ} = \frac{I_{\uparrow} - I_{\downarrow}}{I_{\uparrow} + I_{\downarrow}}$ is the radiation helicity and I is the photocurrent, θ is the incident angle, and n is the index of refraction of Cd_3As_2 . Note that here we normalize C by D to account for the laser intensity change caused by realignment at each incident angle, as both C and D are linear with laser intensity in the range used in our experiment [Fig. 8]. C vanishes when the laser is incident in the $x - z$ plane at $\phi = 0^\circ$ [Fig. 2(h)]. This is also consistent with what is expected from the spin-momentum locking picture, since the injected in-plane spins parallel to the channel do not modulate the measured longitudinal current.

C. Photon energy dependence

To better understand the origin of HDPC, we varied the incident photon energy from 0.77 to 2.5 eV. The measurements were performed by fixing the laser at the contact while rotating the QWP. As shown in Fig. 3(a), photocurrent as a function of α clearly shows a difference at LCP and RCP, at all incident wavelengths. Interestingly, the degree of helicity dependence is greatly enhanced at lower photon energy. C is normalized by D to account for the variation of absorbed laser power. C/D stays at about 2% when photon energy is above 1.8 eV, but increases by a factor of 10 to a remarkably high value of about 20% at 0.77 eV [Fig. 3(b)]. The trend is similar in both devices measured. The photon energy dependent HDPC can be understood by considering the optical transitions as shown in the inset of Fig. 3(b). High energy photons can excite electrons from surface states to bulk states, as well as from bulk to bulk states. At lower photon energies, the bulk to bulk transitions are suppressed, increasing contribution from the surface to bulk transitions. This observation suggests that transitions from low energy surface states likely contribute to the observed HDPC.

IV. DISCUSSION

We first discuss the possible mechanisms for the observed HDPC in our Cd_3As_2 devices. It is now generally accepted that the Cd_3As_2 crystal has inversion symmetry (space group $I4_1/acd$ and point group D_{4h}) [23] and hence CPGE is not allowed in the bulk of the material. Therefore, HDPC is likely originated from the surface

states, which is further supported by the experimental observation that CPGE is enhanced at low energy photoexcitation. We attribute the observed HDPC to CPGE as a result of light induced spin polarization via the surface Fermi arcs. As it was realized earlier on, the paired Weyl points in DSMs do not mean that the surface Fermi arcs connecting oppositely charged Weyl points have zero length, since there are in principle multiple ways to connect those Weyl points [29]. Indeed, the theory of the Fermi arcs in DSMs has been recently discussed in connection to their topological protection property [30]. Fermi arcs have been paramount to understanding the 3D quantum Hall effect [4], high surface conductivity [31], and protection against disorder in DSMs [32, 33]. Fermi arc induced CPGE has been predicted [34] and experimentally probed in a WSM RhSi [35]. These surface states can also lead to CPGE in DSMs, as explained in the following discussion. In equilibrium, the two Fermi arcs at the surface of DSMs are equally spin polarized and carry no net charge current. When the top and bottom surfaces of a DSM slab are decoupled in an optically thick sample, photoexcitation mainly happens close to the top surface. In this case, circularly polarized light selectively excites electrons from one of the Fermi arcs to higher energy states, leading to spin polarization at the top surface [Fig. 4(a)]. CPGE can then be induced by the spin-momentum locking in the spin-polarized Fermi arcs.

To confirm the existence of the surface Fermi arcs and their spin-momentum relations, we first conduct a numerical density functional based calculation of the electronic structure of Cd_3As_2 using local density approximation (LDA) and the full potential linear muffin-tin orbital method [36]. In accordance with previous calculations [23], the Dirac points occur along the $\Gamma - Z$ line of the Brillouin Zone. To perform corresponding surface calculations, we construct a simple 2 orbital tight binding model (see Appendix) that qualitatively reproduces all features of the LDA calculated energy bands including the realization of the Dirac points along [001], shown in Fig. 4(b). To simulate the experimentally grown nanobelt, we construct a superlattice of Cd_3As_2 with primitive translations corresponding to the direct lattice vectors (112) and ($\bar{1}10$) (in units of a,a,c, where experimentally $a=23.88 \text{ \AA}$ and $c/a=2.0127$). The third translation remains the same as in the original lattice, i.e. $(-\frac{1}{2}, \frac{1}{2}, \frac{1}{2})$. We subsequently introduce a slab along the (-1,1,0) comprising of 10 unit cells of such superlattice (60 unit cells of the original structure) for which the

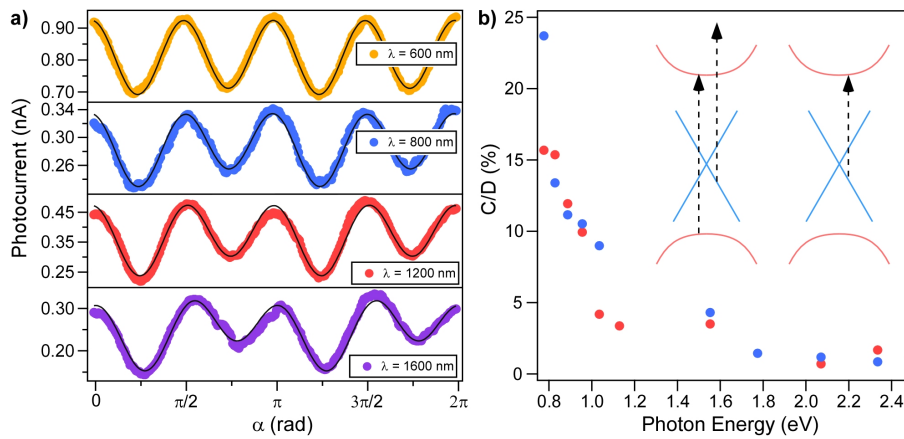


FIG. 3. HDPC at different incident photon energies. (a) HDPC as a function of α for a variety of incident wavelengths. Solid curves are fittings by Eqn. (1). Data depicted is extracted from Device #5. (b) C normalized by D as a function of photon energy extracted from Devices #5 (blue) and #6 (red). Inset: Schematic of optical transitions at high (left) and low (right) photon energies, respectively.

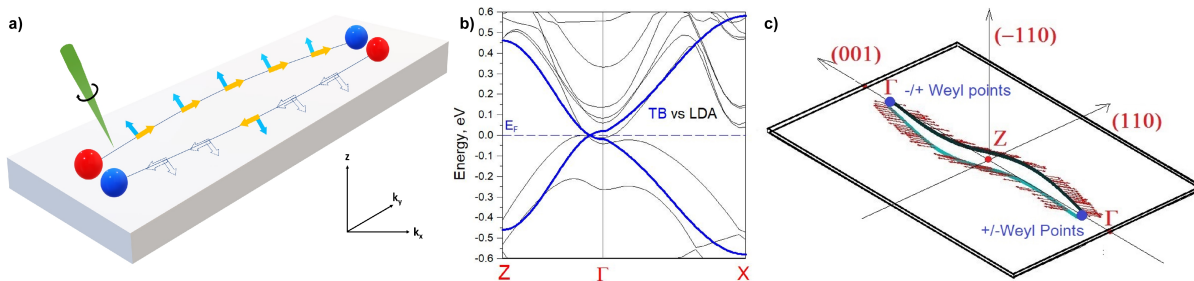


FIG. 4. CPGE via Fermi arcs in Cd_3As_2 . (a) Schematic of spin-momentum locked Fermi arcs under a circularly polarized laser on the top surface of a DSM, drawn in hybrid real-reciprocal coordinates. The red and blue balls represent the projection of Weyl nodes of opposite chirality to the top surface. The blue and yellow arrows indicate the momentum and spin of the electrons in the Fermi arcs. The empty arrows indicate the missing electrons excited by circularly polarized light to higher energy states. (b) Tight binding (TB, blue) and local density approximation (LDA, black) models can both reproduce the Dirac points along $[001]$ in Cd_3As_2 . (c) Calculated Fermi arcs projected onto the $(\bar{1}10)$ surface. Note that the electron spins are oriented in-plane within the surface.

slab energy bands are obtained using the above described 2 orbital tight binding model. The result of such calculation for one (top) surface is shown in Fig. 4(c). The Fermi surface of the slab is comprised of the two bulk Dirac points, each made of two Weyl points of opposite chirality. These points are projected to the surface Brillouin Zone and the Fermi arcs connecting the Weyl points are of opposite chirality. The spin structure of the Fermi arcs is shown at this figure by vectors and is seen to lie within the $(\bar{1}10)$ plane.

We will briefly discuss the Rashba-Edelstein effect and the photo-induced inverse spin Hall effect (PISHE), which can both induce HDPC. No Rashba splitting has been reported in Cd_3As_2 by angle-resolved photoemission spectroscopy (ARPES). The topological surface states, if existing, are also expected to create much more efficient spin generation and HDPC than the Rashba-Edelstein effect [10, 11]. Hence, the Rashba-Edelstein effect is unlikely the dominant mechanism. PISHE is induced by

the diffusion of spins and requires a focused laser [37]. In our case, C/D does not change much with the laser spot size [Fig. 8], indicating it is unlikely caused by PISHE. Additionally, HDPC disappears at normal incidence [Fig. 2(f)] where PISHE should be strongest.

Finally, we discuss a possible reason why CPGE in our Cd_3As_2 devices only occurs when photoexcitation is near the contact, while CPGE in TIs can be observed throughout the device channel [11, 13]. This can be understood by the different bulk conductivities in the two systems. The TI bulk is gapped and hence the spin injection at the TI surface drives an electric current confined at the surface. Therefore, HDPC can be detected even when the light is focused in the middle of the channel in this case. In contrast, the DSM bulk is gapless and hence the CPGE-created current source at the surface can be locally dissipated through the conducting bulk, resulting in nondetectable HDPC away from the contacts. Only when the spin injection is close to the contact can the

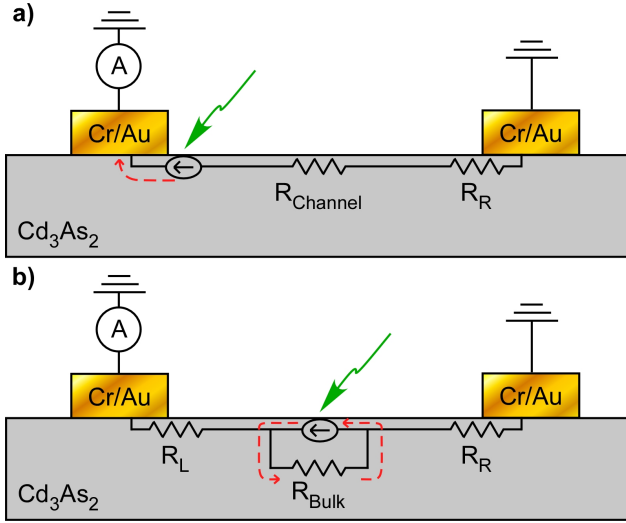


FIG. 5. Circuit model for understanding local CPGE. Equivalent circuit diagrams when circularly polarized photoexcitation is in the vicinity of the contact (a) and away from the contacts (b), respectively. The green arrows indicate the laser position. The red dashed curves indicate the major current flow.

spin induced current be directly collected. In this model, the local circularly polarized photoexcitation generates a constant current source at the surface. If the photoexcitation is near the contact, such a current source can drive charge flow directly into the contact, leading to the observed CPGE [Fig. 5(a)]. However, if the photoexcitation is in the channel far away from the contact, the gapless bulk states in Cd_3As_2 under the surface current source forms a parallel dissipative pathway [Fig. 5(b)]. Thus, only a small portion of the generated current can flow through the more resistive path to the contact and hence CPGE cannot be detected by the preamplifier in this case. Most previous work on CPGE was performed with low spatial resolution, forbidding the observation of such local CPGE in DSMs.

In summary, we have performed spatially and energetically resolved circular polarization dependent photocurrent measurements in Cd_3As_2 nanobelt FETs. The high spatial resolution unambiguously revealed HDPC near the metal contacts. Theoretical calculations are performed to further understand the nature of the topological surface states, where spin-momentum locked Fermi arcs are predicted at the $\{110\}$ surface of the Cd_3As_2 . Our work provides key information on light control over electronic and spintronic properties and broadens the spintronic material candidates.

ACKNOWLEDGMENTS

We thank Valentin Taufour and Rahim Ullah for assistance in XRD characterization. This work was supported by the U.S. National Science Foundation Grants DMR-

2105161 and DMR-2209884. S.Y.S. acknowledges DMR-1832728. W.H. and K.B. acknowledge DMR-1836571. Part of this study was performed at the UC Davis Center for Nano and Micro Manufacturing (CNM2) and the Advanced Materials Characterization and Testing Laboratory (AMCaT). Device fabrication was partially carried out at the Molecular Foundry, which is funded by the Office of Science, Office of Basic Energy Sciences, of the U.S. Department of Energy under Contract No. DE-AC02-05CH11231.

Appendix A: Theoretical Calculations of Surface States

1. Two Orbital Tight Binding Model

A generic $k \cdot p$ model for the Dirac semimetal has been described many times in the literature [38]. It consists of two orbitals with \mathbf{k} dispersions $\pm M(\mathbf{k})$, where $M(\mathbf{k}) = M_0 - M_1(k_x^2 + k_y^2) - M_2k_z^2$, that interact via the matrix element $A(k_x \pm ik_y)$:

$$H(\mathbf{k}) =$$

$$\begin{bmatrix} +M(\mathbf{k}) & A(k_y + ik_x) & 0 & Bk_z \\ A(k_y - ik_x) & -M(\mathbf{k}) & Ck_z & 0 \\ 0 & Ck_z & +M(\mathbf{k}) & -A(k_y - ik_x) \\ Bk_z & 0 & -A(k_y + ik_x) & -M(\mathbf{k}) \end{bmatrix}$$

This model can naturally be utilized to describe the band structure in the vicinity of Dirac points of Cd_3As_2 .

Its tight-binding generalization follows by considering two orbital tight-binding model on Cd_3As_2 lattice given by the primitive translations:

$$A = (1, 0, 0)$$

$$B = (0, 1, 0)$$

$$C = (1/2, 1/2, 1/2)$$

(in units of a, a, c where experimentally $a = 23.88 \text{ a.u.}$ and $c/a = 2.0127$). With the notations for two orbitals $\tau = \pm 1$ and for two spins $\sigma = \pm 1$ at each site, we have non-zero terms of the Hamiltonian:

$$H_{\tau\sigma\tau\sigma}(0) = \sigma\Delta$$

$$H_{\tau\sigma\tau\sigma}(A) = \sigma t_1$$

$$H_{\tau\sigma\tau\sigma}(B) = \sigma t_1$$

$$H_{\tau\sigma\tau\sigma}(C) = \sigma t_2$$

$$H_{\tau\sigma\tau-\sigma}(A) = \tau\lambda/i$$

$$H_{\tau\sigma\tau-\sigma}(B) = \tau\sigma\lambda$$

This produces the terms of the Hamiltonian:

$$\begin{aligned} H_{\tau\sigma\tau\sigma}(\mathbf{k}) &= \sum_{\mathbf{R}} e^{i\mathbf{k}\cdot\mathbf{R}} H_{\tau\sigma\tau\sigma}(\mathbf{R}) = \sigma\Delta + 2\sigma t_1 (\cos k_x + \cos k_y) \\ &\quad + 8\sigma t_2 \cos k_x / 2 \cos k_y / 2 \cos k_z / 2 \\ H_{\tau\sigma\tau-\sigma}(\mathbf{k}) &= \sum_{\mathbf{R}} e^{i\mathbf{k}\cdot\mathbf{R}} H_{\tau\sigma\tau-\sigma}(\mathbf{R}) = 2\tau\lambda (\sin k_x + \sigma i \sin k_y) \end{aligned}$$

At small wavevectors we obtain:

$$H_{\tau\sigma\tau\sigma}(\mathbf{k}) = \sigma\Delta + 4\sigma t_1 + 8\sigma t_2 - \sigma(t_1 + t_2)(k_x^2 + k_y^2) - \sigma t_2 k_z^2$$

$$H_{\tau\sigma\tau-\sigma}(\mathbf{k}) = 2\tau\lambda(k_x + \sigma i k_y)$$

which can be related to the parameters of the $k \cdot p$ Hamiltonian:

$$M_0 = \Delta + 4t_1 + 8t_2$$

$$M_1 = t_1 + t_2$$

$$M_2 = t_2$$

$$A = 2\lambda$$

The comparison between LDA and tight-binding band structures shown in Fig. 1(b) of the main text uses the following parameters:

$$\Delta = 0.18 \text{ eV}$$

$$t_1 = 0.1 \text{ eV}$$

$$t_2 = 0.03 \text{ eV}$$

$$\lambda = 0.05 \text{ eV}$$

2. Fermi Arcs Surface States Calculations

According to experiment, the nanostructure growth occurs along [112] direction with the surface plane corresponding to (-1,1,0). Let us consider the supercell which is described by the primitive translations:

$$\mathbf{A} = \left(-\frac{1}{2}, \frac{1}{2}, \frac{1}{2}\right)$$

$$\mathbf{B} = (-1, 1, 0)$$

$$\mathbf{C} = (1, 1, 2)$$

To get the connection to the original unit cell of Cd_3As_2 set by primitive translations:

$$(1, 0, 0)$$

$$(0, 1, 0)$$

$$\left(\frac{1}{2}, \frac{1}{2}, \frac{1}{2}\right)$$

we need 6 sites of the original lattice to consider as the basis in this supercell:

$$\phi_1 = (0, 0, 0)$$

$$\phi_2 = (1, 0, 0)$$

$$\phi_3 = \left(\frac{1}{2}, \frac{1}{2}, \frac{1}{2}\right)$$

$$\phi_4 = (-1, 0, 0)$$

$$\phi_5 = (0, 1, 1)$$

$$\phi_6 = (1, 1, 1)$$

We further construct the slab structure that extends this supercell 10 times along (-1,1,0) direction (it is made of 60 original unit cells of Cd_3As_2). The tight-binding slab Hamiltonian is then diagonalized, and the Fermi surface corresponding to the one (top) surface of the the slab is plotted in Fig. 4(c) of the main text.

Appendix B: Cd_3As_2 Nanobelt Growth and Device Characteristics

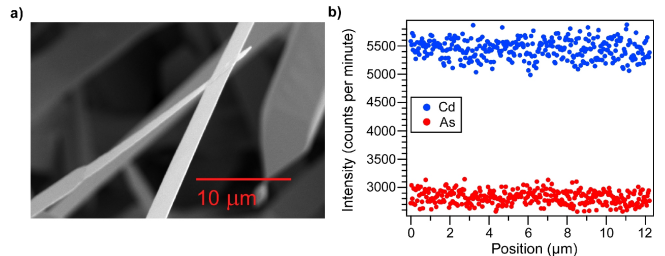


FIG. 6. (a) SEM image of Cd_3As_2 nanostructures on an as-grown substrate. (b) Cross section of the EDS spectrum along the nanobelt showing uniform stoichiometry.

The mobility was calculated by $\mu = \frac{dI_{DS}}{dV_g} \frac{t_{ox}L}{\epsilon_{ox}\epsilon_0 W V_b}$, where $\frac{dI_{DS}}{dV_g}$ is the transconductance, t_{ox} is the oxide thickness, L is the channel length, W is the channel width, ϵ_{ox} is the oxide dielectric constant, ϵ_0 is the permittivity in vacuum, and V_b is the source-drain bias. The carrier concentration was assumed to be uniform over the nanobelt with a thickness of 100 nm. The electron carrier concentrations (n) in the n -type devices were calculated per the expression: $\sigma = nq\mu$, where σ is the conductivity, and q is the fundamental charge.

Device #	T (K)	Conductance (mS)	μ ($\frac{\text{cm}^2}{\text{Vs}}$)	n (cm^{-3})
1	300	1.87	355	1.85×10^{19}
1	78	0.86	3450	1.52×10^{18}
2	300	5.55	278	1.25×10^{19}
2	78	2.52	10100	1.55×10^{17}
3	300	0.74	182	8.47×10^{18}
4	300	6.32	496	4.88×10^{18}
4	78	3.16	2410	5.01×10^{17}

TABLE I. Physical parameters extracted from the field effect characteristics for four representative devices.

Appendix C: Carrier Mobility Extracted from Different Gate Voltage Regimes

The nonlinear gate dependence in Fig. 1(e) indicates different apparent field-effect mobilities in different gate voltage regimes. We note that the apparent mobilities in the regime where carriers are mostly depleted (20 - 40 V) do not represent the true mobility, since the assumption of simple capacitance model to extract the mobility fails. Furthermore, at lower temperatures, the slope changes sign in the negative gate voltage regime, indicating that the chemical potential can be tuned below the charge

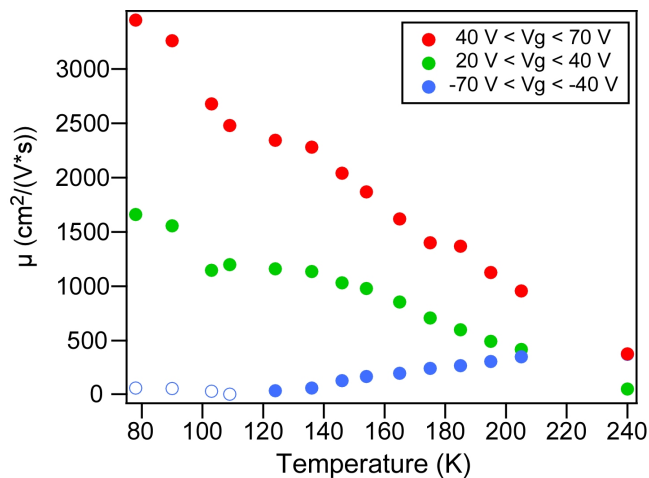


FIG. 7. Apparent field effect carrier mobilities extracted from different gate voltage regimes. Note that the open blue circles represent hole mobility rather than electron mobility.

neutrality point, making holes the majority carriers. At higher temperatures, only positive slopes are observed, likely because the negative gate voltage is insufficient to deplete the thermally activated higher electron density.

Appendix D: Photocurrent Dependence on Laser Intensity and Spot Size

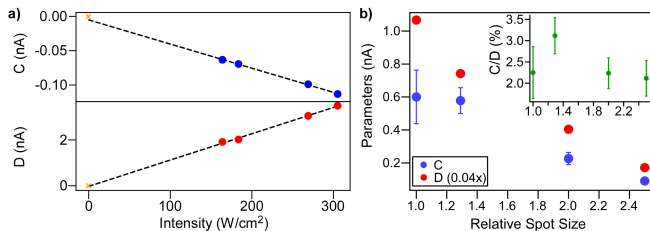


FIG. 8. (a) Both C and D are linear with incident laser intensity. The orange 'x' marks the origin. (b) C and D as a function of spot diameter. D has been scaled down for clarity. Inset: the same C as in (b) but normalized using D .

To shed light on the possible photo-induced inverse spin hall effect (PISHE) mechanism to account for the observed HDPC, we performed the HDPC measurements as a function of laser spot size. PISHE is caused by movement of spins transverse to the spin diffusion current from the focused photoexcitation [37]. We found that C normalized by D does not decrease substantially as the spin density gradient decreases with defocused laser, indicating PISHE is unlikely the dominating mechanism.

-
- [1] D. Pesin and A. H. MacDonald, Spintronics and pseudospintronics in graphene and topological insulators, *Nat. Mater.* **11**, 409 (2012).
- [2] M. He, H. Sun, and Q. L. He, Topological insulator: Spintronics and quantum computations, *Front. Phys.-Beijing* **14**, 1 (2019).
- [3] J.-P. Jay-Gerin, M. Aubin, and L. Caron, The electron mobility and the static dielectric constant of Cd_3As_2 at 4.2 K, *Solid State Commun.* **21**, 771 (1977).
- [4] C. Zhang, Y. Zhang, X. Yuan, S. Lu, J. Zhang, A. Narayan, Y. Liu, H. Zhang, Z. Ni, R. Liu, *et al.*, Quantum Hall effect based on Weyl orbits in Cd_3As_2 , *Nature* **565**, 331 (2019).
- [5] B.-C. Lin, S. Wang, A.-Q. Wang, Y. Li, R.-R. Li, K. Xia, D. Yu, and Z.-M. Liao, Electric control of Fermi arc spin transport in individual topological semimetal nanowires, *Phys. Rev. Lett.* **124**, 116802 (2020).
- [6] T. Liang, Q. Gibson, M. N. Ali, M. Liu, R. Cava, and N. Ong, Ultrahigh mobility and giant magnetoresistance in the Dirac semimetal Cd_3As_2 , *Nat. Mater.* **14**, 280 (2015).
- [7] W. Yu, W. Pan, D. L. Medlin, M. A. Rodriguez, S. R. Lee, Z.-q. Bao, and F. Zhang, π and 4π Josephson Effects Mediated by a Dirac Semimetal, *Phys. Rev. Lett.* **120**,

- 177704 (2018).
- [8] C. Huang, B. T. Zhou, H. Zhang, B. Yang, R. Liu, H. Wang, Y. Wan, K. Huang, Z. Liao, E. Zhang, *et al.*, Proximity-induced surface superconductivity in Dirac semimetal Cd_3As_2 , *Nat. Commun.* **10**, 2217 (2019).
- [9] N. Li, Z.-B. Tan, J.-J. Chen, T.-Y. Zhao, C.-G. Chu, A.-Q. Wang, Z.-C. Pan, D. Yu, and Z.-M. Liao, Gate modulation of anisotropic superconductivity in Al-Dirac semimetal Cd_3As_2 nanoplate-Al Josephson junctions, *Supercond. Sci. Tech.* **35**, 044003 (2022).
- [10] X. Peng, Y. Yang, R. R. Singh, S. Y. Savrasov, and D. Yu, Spin generation via bulk spin current in three-dimensional topological insulators, *Nat. Commun.* **7**, 10878 (2016).
- [11] J. McIver, D. Hsieh, H. Steinberg, P. Jarillo-Herrero, and N. Gedik, Control over topological insulator photocurrents with light polarization, *Nat. Nanotechnol.* **7**, 96 (2012).
- [12] Y. Pan, Q.-Z. Wang, A. L. Yeats, T. Pillsbury, T. C. Flanagan, A. Richardella, H. Zhang, D. D. Awschalom, C.-X. Liu, and N. Samarth, Helicity dependent photocurrent in electrically gated $(\text{Bi}_{1-x}\text{Sb}_x)_2\text{Te}_3$ thin films, *Nat. Commun.* **8**, 1037 (2017).
- [13] D.-X. Qu, X. Che, X. Kou, L. Pan, J. Crowhurst, M. R. Armstrong, J. Dubois, K. L. Wang, and G. F. Chapline, Anomalous helicity-dependent photocurrent in the topological insulator $(\text{Bi}_{0.5}\text{Sb}_{0.5})_2\text{Te}_3$ on a GaAs substrate, *Phys. Rev. B* **97**, 045308 (2018).
- [14] L. Yang, Z. Liu, Y. Sun, H. Peng, H. Yang, T. Zhang, B. Zhou, Y. Zhang, Y. Guo, M. Rahn, *et al.*, Weyl semimetal phase in the non-centrosymmetric compound TaAs, *Nat. Phys.* **11**, 728 (2015).
- [15] F. De Juan, A. G. Grushin, T. Morimoto, and J. E. Moore, Quantized circular photogalvanic effect in Weyl semimetals, *Nat. Commun.* **8**, 15995 (2017).
- [16] C. Le and Y. Sun, Topology and symmetry of circular photogalvanic effect in the chiral multifold semimetals: a review, *J. Phys.-Condens. Mat.* **33**, 503003 (2021).
- [17] G. Liang, G. Zhai, J. Ma, H. Wang, J. Zhao, X. Wu, and X. Zhang, Strain-induced circular photogalvanic current in Dirac semimetal Cd_3As_2 films epitaxied on a GaAs (111) B substrate. *Nanoscale*, **14**(6), 2383–2392 (2022).
- [18] P. Schönherr and T. Hesjedal, Structural properties and growth mechanism of Cd_3As_2 nanowires, *Appl. Phys. Lett.* **106** (2015).
- [19] K. Zhang, H. Pan, M. Zhang, Z. Wei, M. Gao, F. Song, X. Wang, and R. Zhang, Controllable synthesis and magnetotransport properties of Cd_3As_2 Dirac semimetal nanostructures, *RSC Adv.* **7**, 17689 (2017).
- [20] K. Park, M. Jung, D. Kim, J. R. Bayogan, J. H. Lee, S. J. An, J. Seo, J. Seo, J.-P. Ahn, and J. Park, Phase controlled growth of Cd_3As_2 nanowires and their negative photoconductivity, *Nano Lett.* **20**, 4939 (2020).
- [21] W.-Z. Zheng, T.-Y. Zhao, A.-Q. Wang, D.-Y. Xu, P.-Z. Xiang, X.-G. Ye, and Z.-M. Liao, Strain-gradient induced topological transition in bent nanoribbons of the Dirac semimetal Cd_3As_2 , *Phys. Rev. B* **104**, 155140 (2021).
- [22] Q. Zheng, T. Qin, W. Li, X. Wang, Y. Huang, and Z. Liu, Astigmatism analysis and correction method introduced by an inclined plate in a convergent optical path, *Appl. Optics* **60**, 875 (2021).
- [23] M. N. Ali, Q. Gibson, S. Jeon, B. B. Zhou, A. Yazdani, and R. J. Cava, The crystal and electronic structures of Cd_3As_2 , the three-dimensional electronic analogue of graphene, *Inorg. Chem.* **53**, 4062 (2014).
- [24] E. Zhang, Y. Liu, W. Wang, C. Zhang, P. Zhou, Z.-G. Chen, J. Zou, and F. Xiu, Magnetotransport properties of Cd_3As_2 nanostructures, *ACS Nano* **9**, 8843 (2015).
- [25] Y. Hou, R. Wang, R. Xiao, L. McClintock, H. Clark Travaglini, J. Paulus Francia, H. Fetsch, O. Erten, S. Y. Savrasov, B. Wang, *et al.*, Millimetre-long transport of photogenerated carriers in topological insulators, *Nat. Commun.* **10**, 5723 (2019).
- [26] D. Fu, J. Zou, K. Wang, R. Zhang, D. Yu, and J. Wu, Electrothermal dynamics of semiconductor nanowires under local carrier modulation, *Nano Lett.* **11**, 3809 (2011).
- [27] C. Kastl, T. Guan, X. He, K. Wu, Y. Li, and A. Holleitner, Local photocurrent generation in thin films of the topological insulator Bi_2Se_3 , *Appl. Phys. Lett.* **101** (2012).
- [28] J. Yu, Y. Chen, S. Cheng, and Y. Lai, Spectra of circular and linear photogalvanic effect at inter-band excitation in $\text{In}_0.15\text{Ga}_{0.85}\text{As}/\text{Al}_0.3\text{Ga}_{0.7}\text{As}$ multiple quantum wells, *Physica E* **49**, 92 (2013).
- [29] A. C. Potter, I. Kimchi, and A. Vishwanath, Quantum oscillations from surface Fermi arcs in Weyl and Dirac semimetals, *Nat. Commun.* **5**, 5161 (2014).
- [30] M. Kargarian, M. Randeria, and Y.-M. Lu, Are the surface Fermi arcs in Dirac semimetals topologically protected?, *P. Natl. Acad. Sci. USA* **113**, 8648 (2016).
- [31] M. J. Gilbert, Topological electronics, *Commun. Phys.* **4**, 70 (2021).
- [32] B. Focassio, G. R. Schleder, A. Pezo, M. Costa, and A. Fazzio, Dual topological insulator device with disorder robustness, *Phys. Rev. B* **102**, 045414 (2020).
- [33] S. Tang, W. Chen, Q. Ye, Z. Liu, Q. Wu, Y. Du, X. Zhou, and X. Xiao, Electron transport probing the electrically tunable topological phase transition in a Dirac semimetal, *Phys. Rev. B* **104**, 205427 (2021).
- [34] G. Chang, J.-X. Yin, T. Neupert, D. S. Sanchez, I. Belopolski, S. S. Zhang, T. A. Cochran, Z. Chéng, M.-C. Hsu, S.-M. Huang, *et al.*, Unconventional photocurrents from surface Fermi arcs in topological chiral semimetals, *Phys. Rev. Lett.* **124**, 166404 (2020).
- [35] D. Rees, B. Lu, Y. Sun, K. Manna, R. Özgür, S. Subedi, H. Borrmann, C. Felser, J. Orenstein, and D. H. Torchinsky, Direct measurement of helicoid surface states in RhSi using nonlinear optics, *Phys. Rev. Lett.* **127**, 157405 (2021).
- [36] S. Y. Savrasov, Linear-response theory and lattice dynamics: A muffin-tin-orbital approach, *Phys. Rev. B* **54**, 16470 (1996).
- [37] K. W. Tang, B. M. Wang, H. C. Travaglini, and D. Yu, Modeling of the photocurrent induced by inverse spin Hall effect under local circularly polarized photoexcitation, *Phys. Rev. B* **104**, 205413 (2021).
- [38] Z. Wang, H. Weng, Q. Wu, X. Dai, and Z. Fang, Three-dimensional Dirac semimetal and quantum transport in Cd_3As_2 , *Phys. Rev. B* **88**, 125427 (2013).